




ARTICLE



<https://doi.org/10.1038/s41467-022-29863-8>

OPEN

# Lateral growth of cylinders

Hui Sun <sup>1✉</sup>, Shuai Chen <sup>2,3</sup>, Xiao Li<sup>1</sup>, Ying Leng<sup>1</sup>, Xiaoyan Zhou<sup>1</sup> & Jianzhong Du <sup>2,3✉</sup>

The precise control of the shape, size and microstructure of nanomaterials is of high interest in chemistry and material sciences. However, living lateral growth of cylinders is still very challenging. Herein, we propose a crystallization-driven fusion-induced particle assembly (CD-FIPA) strategy to prepare cylinders with growing diameters by the controlled fusion of spherical micelles self-assembled from an amphiphilic homopolymer. The spherical micelles are heated upon glass transition temperature ( $T_g$ ) to break the metastable state to induce the aggregation and fusion of the amorphous micelles to form crystalline cylinders. With the addition of extra spherical micelles, these micelles can attach onto and fuse with the cylinders, showing the living character of the lateral growth of cylinders. Computer simulations and mathematical calculations are preformed to reveal the total energy changes of the nanostructures during the self-assembly and CD-FIPA process. Overall, we demonstrated a CD-FIPA concept for preparing cylinders with growing diameters.

<sup>1</sup>State Key Laboratory of High-Efficiency Coal Utilization and Green Chemical Engineering, Ningxia University, 750021 Yinchuan, China. <sup>2</sup>Department of Gynaecology and Obstetrics, Shanghai Fourth People's Hospital, School of Medicine, Tongji University, 200434 Shanghai, China. <sup>3</sup>Department of Polymeric Materials, School of Materials Science and Engineering, Tongji University, 4800 Caoan Road, 201804 Shanghai, China. ✉email: [sunhui@nxu.edu.cn](mailto:sunhui@nxu.edu.cn); [jzdu@tongji.edu.cn](mailto:jzdu@tongji.edu.cn)

Macromolecular self-assembly is a powerful tool to fabricate functional soft nanomaterials with diverse morphologies including spherical micelles, cylindrical micelles, vesicles and nanobowls, etc.<sup>1–6</sup>. Among them, cylindrical micelles, also known as cylinders, are appealing and versatile due to their unique serpentine conformation and adjustable aspect ratio comparing with their spherical counterparts. These cylinders have shown considerable potentials in cellular uptake and *in vivo* drug delivery due to their high aspect ratio<sup>7–10</sup>. The control of geometric size such as the length and diameter of cylinders is very important and has drawn much attention in the last decade<sup>11–14</sup>. Traditional self-assembly of amphiphilic polymers can regulate the length and diameter of cylinders by changing the chemical composition of polymers, such as the length of hydrophobic block. Taking advantage of the “living” characteristic, the crystallization-driven self-assembly (CDSA) strategy has an aptitude for the control of the length of cylinders<sup>15–17</sup>. Upon addition of polymers, the crystalline or semicrystalline segments crystallized along with the core and guarantee the living longitudinal growth of cylinders<sup>18–20</sup>. For instance, Manners and coworkers developed seeded growth of cylindrical micelles based on the highly crystalline poly(ferrocenyldimethylsilane) (PFS)<sup>21</sup>, and the cylindrical micelles could grow on different manners, such as from both ends<sup>22</sup>, from one end<sup>23</sup> and using different blocks<sup>24</sup>. O’Reilly et al. prepared biodegradable cylinders with controlled length from the semicrystalline polymers including poly(L-lactide) (PLLA)<sup>25</sup>, poly( $\epsilon$ -caprolactone) (PCL)<sup>26,27</sup> based block copolymers via CDSA benefiting from the crystalline property of PLLA and PCL. Recently, Lin and coworkers studied the controlled growth and termination of cylinders self-assembled from liquid-crystallization-driven self-assembly of poly( $\gamma$ -benzyl-L-glutamate)-*block*-poly(*N*-isopropyl acrylamide) (PBLG-*b*-PNIPAM) from both of theoretical and experimental aspect<sup>28</sup>. However, the lateral growth of cylinders is still challenging. Despite the changing of the length of the hydrophobic or the crystalline blocks to control the diameter of cylinders, the living lateral growth of cylinders is still hard to achieve.

The fusion and assembly of particles is an emerging method to fabricate nanomaterials with precisely controlled anisotropy or highly ordered structures<sup>29–33</sup>. For instance, Yuan and coworkers fabricated AB<sub>*n*</sub>-type colloidal particles by polymerization-induced particle-assembly using a linear ABC triblock terpolymer, and the number of *n* could be controlled between 2 and 6 by tuning the volume ratio of different blocks<sup>29</sup>. O’Reilly et al. investigated the polymerization-induced fusion behaviors of polymersomes<sup>33</sup>. They found that the membrane tension of the polymer vesicles with the continued polymerization was the main driving force for the fusion of polymersomes to form tubesomes. Recently, our group proposed a FIPA strategy to prepare tetrapod polymersomes and micelle clusters by spherical polymersomes and micelles<sup>30</sup>. The formation of either tetrapod polymersomes or micelle clusters is a matter of balance between pro-fusion and anti-fusion forces provided by the different components in the polymer. One step further, giant polymer vesicles with a lattice-like membrane were also obtained by the FIPA of small-sized vesicles<sup>34</sup>.

In this work, we propose a CD-FIPA strategy to achieve the living lateral growth of cylinders via the hierarchical self-assembly of a semicrystalline homopolymer, as shown in Fig. 1. The amphiphilic homopolymer poly(2-(4-(phenyldiazenyl)phenoxy) ethyl methacrylate) (PAzoMA) with only hydrophilic terminal carboxylic group and crystalline azobenzene pendants was synthesized via reversible addition-fragmentation chain transfer (RAFT) polymerization. Upon addition of water to the solution of PAzoMA, spherical micelles were obtained. However, the colloidal stability of the micelles is broken when the temperature rises to 75 °C (above the *T*<sub>g</sub> of PAzoMA), leading to the aggregation

and fusion of the micelles, as well as the formation of cylinders. Interestingly, the amorphous to crystalline transformation occurred between spherical micelles and cylinders due to the regular rearrangement of the azobenzene pendants since the incubation temperature is higher than the *T*<sub>g</sub> (63.1 °C) of PAzoMA to ensure the sufficient motion of azobenzene pendants. More importantly, the diameter of the cylinders can be controlled from 68.6 ± 12.3 to 137.6 ± 17.3 nm with the addition of spherical micelles to the solution of cylinders. In addition, the cross-section area of the cylinders shows a linear relationship with the mass ratio of added spherical micelles to cylinders, indicating that all the spherical micelles added are fused with the cylinders. Moreover, computer simulation and theoretical calculation further confirm that the CD-FIPA of spherical micelles to form cylinders is a process of reducing the energy of the system, resulting in a more stable thermodynamic state.

## Results and discussion

**Synthesis, characterization, and self-assembly of PAzoMA.** The PAzoMA was synthesized via RAFT polymerization using 4-cyano-4-((phenylcarbonothioyl)thio)pentanoic acid (CPAD) as chain transfer agent. The synthetic route of AzoMA monomer and PAzoMA was presented in Supplementary Fig. 1. The nuclear magnetic resonance (NMR) and high resolution mass spectra in Supplementary Figs. 2 and 3a–c demonstrated the successful synthesis of the AzoMA monomer. The disappearance of the signal of the double bond in the NMR spectrum in Supplementary Fig. 4a indicated the entire consumption of AzoMA monomer, and the <sup>13</sup>C NMR spectra in Supplementary Fig. 4b further confirmed the successful synthesis of PAzoMA. The degree of polymerization of PAzoMA was 21, as calculated from the conversion of the monomer based on the NMR spectrum in Supplementary Fig. 4a. The number average molecular weight of PAzoMA was calculated to be 6900. The gel permeation chromatography (GPC) trace of PAzoMA in Supplementary Fig. 5 revealed a molecular weight of 6700 with a low polydispersity index (*D*) of 1.11, which was in accordance with the molecular weight calculated from the NMR spectrum.

The thermal property of PAzoMA was investigated by differential scanning calorimetry (DSC), as illustrated in Supplementary Fig. 6. The *T*<sub>g</sub> of PAzoMA was 63.1 °C, while the melting point was 100.4 °C. The melting enthalpy ( $\Delta H_m$ ) of PAzoMA was measured to be 6.62 J g<sup>-1</sup>, which is much lower than that of reported typical crystalline and azobenzene-containing polymers<sup>35,36</sup>. Assuming that a purely crystalline sample has a typical value of  $\Delta H_m \approx 150–300$  J g<sup>-1</sup>,<sup>37</sup> the crystallinity of PAzoMA is estimated to be ~4–8%. The crystal structure of PAzoMA at different temperatures (25, 50, 75, 100 and 110 °C) was characterized by powder X-ray diffraction (XRD), as shown in Supplementary Fig. 7. There are three weak diffraction peaks centered at  $2\theta$  of 31.6°, 36.5°, and 45.1°, corresponding to the (120), (114), and (700) plane of PAzoMA<sup>38–40</sup>. When the temperature is elevated above the phase transition temperature of PAzoMA, the diffraction peaks in Supplementary Fig. 7 vanished, demonstrating the disappearance of the ordered structure. In addition, no liquid crystalline phase was observed in polarizing optical microscope (POM) images at 110 °C or cooling to 25 °C, as illustrated in Supplementary Fig. 8a, b, which might be ascribed to the lack of flexible or polar groups at the para position of azobenzene.

The PAzoMA has an ultralow hydrophilic content of 0.65% as its backbone and pendants are hydrophobic, while only the terminal carboxyl group is hydrophilic. Previous studies showed that very small amount of terminal groups could induce the self-assembly of amphiphilic homopolymers<sup>41,42</sup>. The PAzoMA could

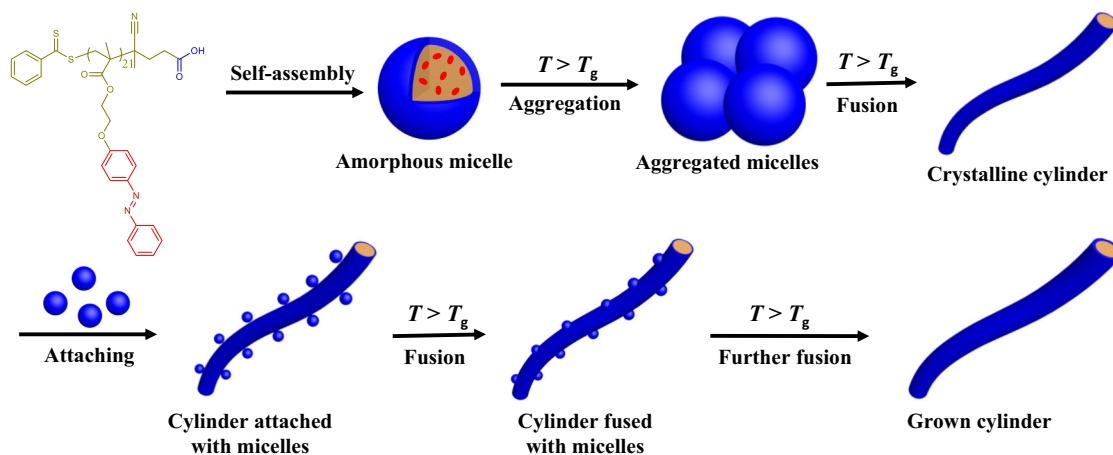


**Fig. 1 Self-assembly of PAzoMA to form spherical micelles and living lateral growth of cylinders by CD-FIPA of micelles.** PAzoMA homopolymer can self-assemble into amorphous spherical micelles, which aggregate and fuse to form crystalline cylinders when incubated at 75 °C. With the addition of spherical micelles, the micelles attach onto and fuse with the cylinders, leading to the living lateral growth of cylinders.

self-assemble into spherical micelles with a hydrodynamic diameter ( $D_h$ ) of 33 nm and low polydispersity (PD) of 0.107 at a water dropping rate of 0.5 mL min<sup>-1</sup>, as measured by dynamic light scattering (DLS, Supplementary Fig. 9). In addition, the Zeta potential of the micelles was measured to be -23.9 mV (Supplementary Fig. 10), demonstrating that the terminal carboxyl groups covered the surface of the micelles, which kept the electrosteric stability of the micelles. The TEM image in Supplementary Fig. 11 revealed the spherical morphology of the micelles. The formation of the spherical micelles is kinetically controlled. When decreasing the water dropping rate to 0.1 mL min<sup>-1</sup>, large compound micelles were obtained (Supplementary Fig. 12). After the formation of micelles, the UV-vis adsorption peak of PAzoMA was red shifted from 343 to 385 nm (Supplementary Fig. 13), indicating the strong  $\pi$ - $\pi$  interaction between azobenzene pendants<sup>43</sup>.

#### CD-FIPA of amorphous micelles to form crystalline cylinders.

Considering that the electrosteric stability of the micelles was mainly provided by the negative charge on the surface, we speculated that the thermo-treatment might disturb the stability of the micelles, which was a commonly used method to break the stability of colloids<sup>44</sup>. So the spherical micelle solution with a concentration of 0.12 mg mL<sup>-1</sup> was incubated in water bath at 75 °C to induce the aggregation and fusion of the micelles. As shown in Fig. 2a, the small spherical micelles aggregated and fused to form large particles with irregular morphology when incubated for 15 min. The DLS and Zeta potential results in Supplementary Figs. 9 and 10 further confirmed the aggregation of the micelles since the diameter increased to 68 nm. As the incubation time increased to 30 min, the irregular aggregates connected into a necklace to decrease the surface free energy and part of the polymers softened and connected to form the continuous structure, as pointed by the red arrow in Fig. 2b. Surprisingly, the connected micelles was semicrystalline rather than the amorphous state of the original spherical micelles (Supplementary Fig. 14), as shown in the selected area electron diffraction (SAED) pattern in Fig. 2c, demonstrating the regular rearrangement of the azobenzene pendants when incubated at 75 °C.

With the increase of incubation time, the connected micelles were fused to form cylindrical structures attached with fragments of spherical micelles, as presented in Fig. 2d, e. Besides, the electron diffraction signal in Fig. 2f demonstrated the

preservation of the crystal structure during incubation. When the incubation time was extended to 3 h, the aggregates attached onto the cylindrical structures disappeared and the cylinders were formed by the CD-FIPA of spherical micelles. As shown in Fig. 2g, the high contrast areas pointed by the red circles were the cores of the spherical micelles that were not completely fused. In addition, there were still unfused spherical micelles in the solution. With the further prolongation of incubation time to 6 h, the 'mature' cylinders were formed (Fig. 2h), and the DLS and Zeta potential measurements revealed a  $D_h$  of 327 nm and a similar Zeta potential of -22.6 mV to the spherical micelles (Supplementary Figs. 9 and 10).

To investigate the influence of the concentration of spherical micelles on the particle fusion rate, the solution of spherical micelles was concentrated to 0.25 mg mL<sup>-1</sup> and incubated at 75 °C. As shown in Supplementary Fig. 15a-c, the particle fusion rate barely changed, which might be controlled by the crystallization process of the homopolymer. Supplementary TEM image of the preformed cylinders at low magnification was provided in Supplementary Fig. 16, revealing a diameter of 56.2-80.4 nm (average diameter of 68.6 ± 12.3 nm) and a length of 1110-1940 nm. The cylinder has gradient diameter with thick head and thin tail, which is formed at the very beginning of the formation of cylinders, as illustrated in Supplementary Fig. 17. The morphology of the cylinders was similar to the previously reported cylinders that obtained via counterion-mediated particle fusion of spherical micelles self-assembled from ion-containing block copolymers<sup>45</sup>. In addition, the diffraction spots in SAED pattern in Fig. 2i belong to the (113), (114), (700) planes of PAzoMA, corresponding to  $d$ -spacing of 0.331, 0.234 and 0.202 nm, respectively, which are consistent with the XRD results.

The proposed mechanism of the transformation from amorphous to crystalline during CD-FIPA is illustrated in Fig. 3. When the PAzoMA self-assembles into micelles, the polymer chains and the azobenzene pendants are arranged randomly, leading to the amorphous state of the micelles. As the temperature rises above the  $T_g$  of the PAzoMA, the micelles are fused to form necklace-like structure (Fig. 2b, e) and immature cylinders due to the disturbance of the electrosteric stability of the micelle solution, while the chain mobility of the PAzoMA significantly increases to promote the rearrangement of azobenzene pendants at the same time. Therefore, the obtained cylinders are crystalline instead of the amorphous state of the spherical micelles. With the prolonged incubation of the immature cylinders at 75 °C ( $>T_g$ ), the micelles attached onto the cylinder

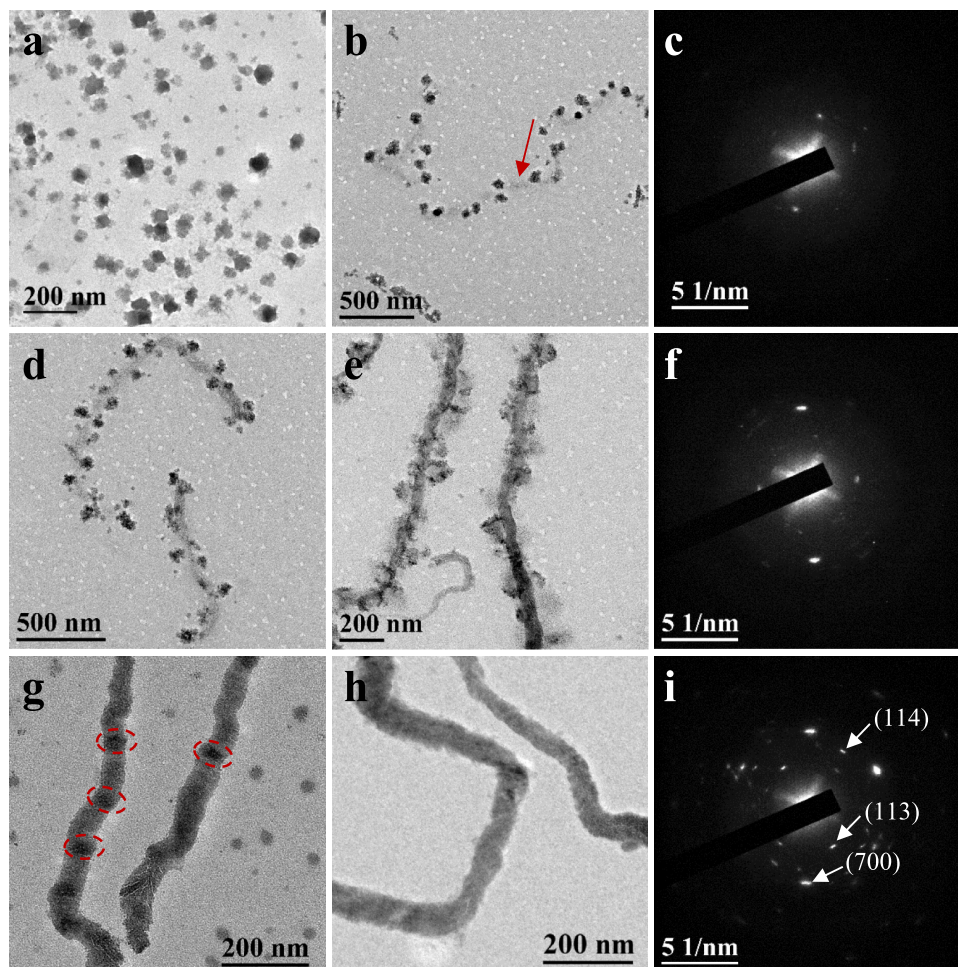


**Fig. 2** Formation of semicrystalline cylinders via CD-FIPA of spherical micelles. **a** Incubated for 15 min, **b** 30 min, and **c** corresponding SAED pattern; **d** 60 min, **e** 90 min, and **f** corresponding SAED pattern; **g** 3 h, **h** 6 h, and **i** corresponding SAED pattern.

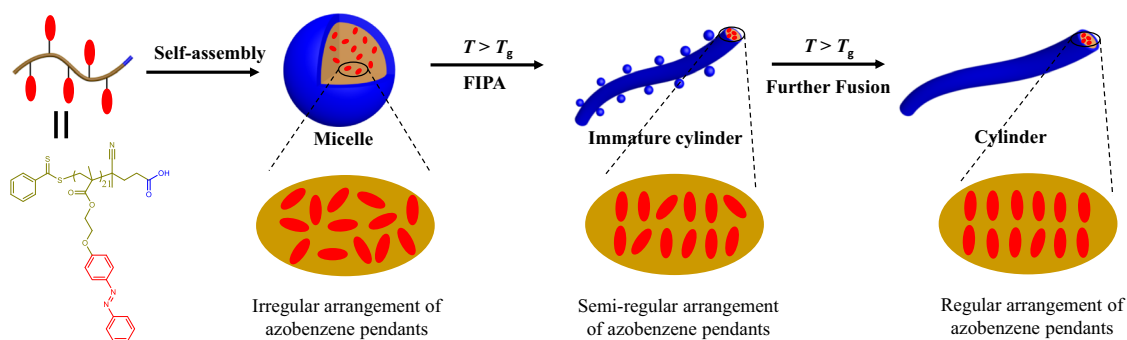


**Fig. 3** Proposed mechanism of the transformation from amorphous micelles to crystalline cylinders during CD-FIPA. The azobenzene pendants arrange randomly in the amorphous micelles. When incubated at 75 °C (higher than the  $T_g$  of PAzoMA), the chain mobility of PAzoMA significantly increases, leading to the regular arrangement of azobenzene pendants and crystalline structure of cylinders.

are entirely fused with the cylinders to form mature cylinders. The rearrangement of the azobenzene pendants and the CD-FIPA process should occur simultaneously.

**Living lateral growth of cylinders.** Living lateral growth of cylinders is still challenging despite the changing of the length of hydrophobic chains to control the diameter of cylinders. Herein, we intended to conquer this challenge by the CD-FIPA of spherical micelles. As shown in Fig. 4a, the cylinders and

spherical micelles were mixed and incubated at 75 °C. After 60 min, the micelles aggregated to form irregular aggregates and attached onto the surface of preformed cylinders (Fig. 4b). The darkness of the aggregates is intensive after attaching onto the cylinders, which is ascribed to the crystallization of the aggregates during the incubation process, as shown in Supplementary Fig. 18a, b. When the incubation time was prolonged to 3 h, the irregular aggregates were entirely fused with the preformed cylinders (Fig. 4c). In the previous section, we have proven that the formation of cylinders is due to the crystallization-driven



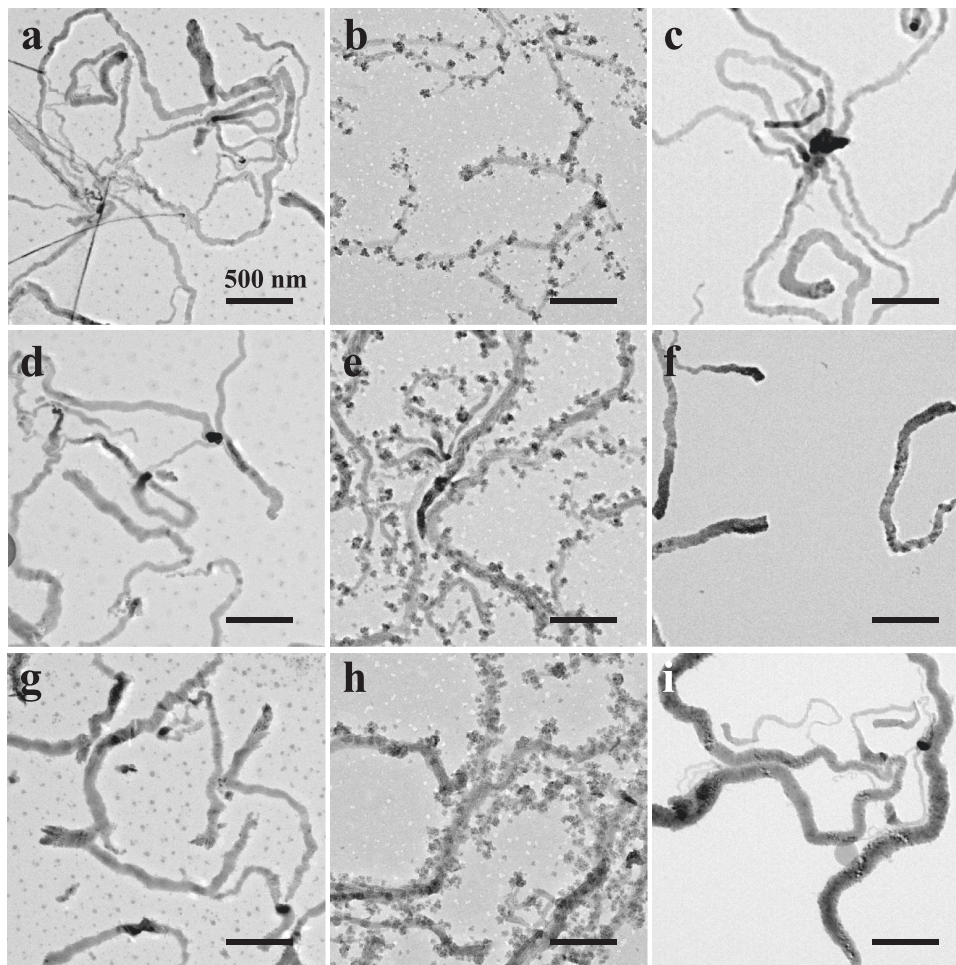


**Fig. 4** The living lateral growth of cylinders by CD-FIPA. **a**, **d**, and **g** the mixture of spherical micelles and cylinders before incubation; **b**, **e**, and **h** incubation at 75 °C for 60 min; **c**, **f**, and **i** incubation at 75 °C for 3 h.

aggregation and fusion of spherical micelles, which is also responsible for the lateral growth of cylinders. To further prove this hypothesis, the mixed solution of spherical micelles and cylinders was kept at 25 °C for 3 h. As illustrated in Supplementary Fig. 19, the added spherical micelles did not attach on the cylinders. In addition, the laterally grown sections of cylinders are also crystalline, as confirmed by the SAED pattern in Supplementary Fig. 18b.

In order to achieve the living lateral growth of the cylinders, we repeated the above micellar addition procedure for two more times. As shown in Fig. 4d–f, the spherical micelles aggregated, attached and fused with the cylinders in a similar behavior. Upon addition of the spherical micelle solution for the third time, the diameter of the cylinders further increased (Fig. 4g–i), demonstrating the validity of the living lateral growth of the cylinders via the CD-FIPA of spherical micelles. The diameter of the cylinders increased to  $94.1 \pm 12.8$  nm, and further increased to  $118.3 \pm 15.6$  and  $137.6 \pm 17.3$  nm after growth, respectively. More TEM images at low and high resolutions were provided in Supplementary Fig. 20a–f. The epitaxial growth of the cylinders was not observed from TEM images since the added spherical micelles attached onto the surface of the preformed cylinders instead of from the termini of the cylinders. Besides, the length of the cylinders was measured to be 1200–1920 nm, which was consistent with that before growth, further excluding the termini growth of the cylinders. Furthermore, the laterally grown cylinders inherited the gradient diameter features of the preformed cylinders, indicated

that the added micelles attached onto and fused with the cylinders evenly, further proving the validity of the lateral growth of cylinders. There are few thin cylinders in the lateral growth process of cylinders, as illustrated in Fig. 4d, i, which is ascribed to the entire consumption of added spherical micelles, so there are no micelles attached onto the surface of the cylinders, as pointed by the red arrows in Supplementary Fig. 21. It is noteworthy that thin cylinders were reduced when the mass ratio of added spherical micelles to cylinders was increased to two times of that before. As presented in Supplementary Fig. 22a, b, the diameter of the cylinders is more uniform than before and thin cylinders disappeared, demonstrating the controllability of the living lateral growth of cylinders by CD-FIPA.

To reveal the living growing rule of the CD-FIPA of the spherical micelles on the surface of cylinders, we theoretically analyzed the relationship between the diameters ( $d$ ) of the cylinders and the mass ratio of added micelles to cylinders (defined as  $n$ ,  $n = 0$  representing the preformed cylinders). In principle, the square of the diameter of grown cylinders should have a linear relationship with  $(n + 1)$ , as shown in Fig. 5a. The deduction details are presented in Supplementary information. In reality, the experimental results confirmed this mathematical prediction. As illustrated in Fig. 5b, theoretically, the diameter of the grown cylinders shows a square root relationship with  $(n + 1)$ . Indeed, the experimental results were well fitted with the theoretical prediction. Similarly, the cross-sectional area ( $S_c$ ) of the cylinders showed a linear relationship with  $(n + 1)$ , as

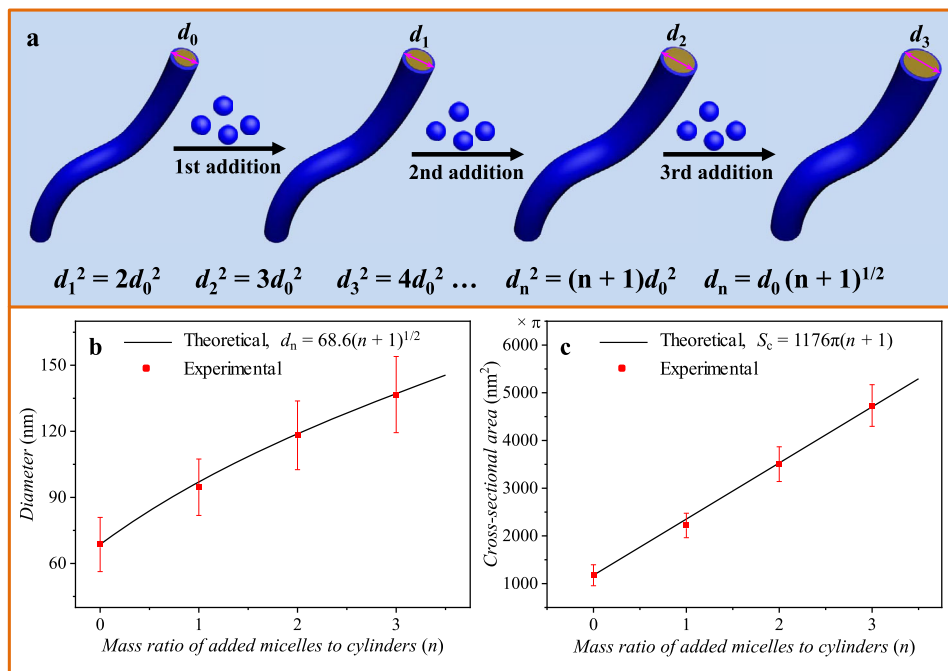


**Fig. 5** Quantitative analysis of the living lateral growth of the cylinders. **a** Schematic illustration of the living lateral growth of cylinders, and the relationship between **b** diameter and **c** cross-sectional area of the cylinders and the mass ratio of added micelles to cylinders. The error bars in **b** and **c** are calculated by measuring the diameter of cylinders.

presented in Fig. 5c. In the previous section, we have confirmed that the length of the cylinders remains the same before and after growth. Assuming that the density of the spherical micelles and cylinders remained unchanged before and after growth of cylinders, the total volume of the cylinders should have a linear relationship with  $(n + 1)$ , demonstrating that all the spherical micelles were attached onto and fused with the cylinders, which could also be confirmed by the TEM images in Fig. 4c, f and i.

**Computer simulations to reveal the energy fluctuation during self-assembly and CD-FIPA.** The conformation optimization of the PAzoMA and the energy evolution of the system during the self-assembly and CD-FIPA processes were monitored by molecular dynamics (MD) simulation by Materials Studio 2017 according to our previous study<sup>46</sup>. MD simulation is a thermodynamic calculation method which adopted Newton's equations of motion for the calculation of all-atom trajectories, thus acquiring the thermodynamic quantities and other macroscopic properties of different molecular systems<sup>47</sup>. Typically, the structural changes and the energy evolution reflect the thermodynamic state of the system; the decreasing of the total energy of the "cell" indicates a more stable thermodynamic state under simulated forces. The details of the simulation settings were presented in the Supplementary information. First, we investigated the self-assembly of PAzoMA<sub>21</sub> to form spherical micelles by MD simulation. As shown in Supplementary Fig. 23, the model of PAzoMA<sub>21</sub> was built and optimized by Forcite, and the initial state and the output state of the "cell" containing 5 model chains were also presented in Supplementary Fig. 24a, b, revealing the optimization of the geometry of the molecular chains to decrease the energy of the system. In addition, the change of the total energy ( $\Delta E$ ) of the "cell" was calculated to be  $-12,953.2 \text{ kcal mol}^{-1}$  (Supplementary Fig. 25), demonstrating the decrease of the total energy during self-assembly to reach a more stable thermodynamic state.

To investigate the geometry optimization of PAzoMA and the energy evolution during CD-FIPA process, MD simulation was further conducted by constructing a crystalline cell consisting of

one PAzoMA<sub>5</sub> chain to simplify the calculation process. The Forcite-optimized model of PAzoMA<sub>5</sub> was illustrated in Supplementary Fig. 26, and the corresponding initial state and output state of the molecular geometry at different temperatures were also investigated and presented in Supplementary Fig. 27a–d. As shown in Fig. 6, the energy evolution of the "cell" and the summary of the energy state, as well as the change of  $\Delta E$  at different temperatures were also obtained. The total energy of the "cell" is  $9791.9 \text{ kcal mol}^{-1}$ , which descended to different levels at 298, 348, and 373 K (Fig. 6a–c). However, the  $\Delta E$  reached a lowest state at 348 K, which is slightly higher than the  $T_g$  of the PAzoMA, corresponding to a  $\Delta E$  of  $-1683.6 \text{ kcal mol}^{-1}$ , as illustrated in Fig. 6d. The lowest energy state of the "cell" at 348 K demonstrated that the system reached the most stable thermodynamic state, so we conducted CD-FIPA at this temperature.

**Mechanism of CD-FIPA.** We have confirmed that all the spherical micelles were fused to form cylinders. Considering that the specific surface area of the spherical micelles was significantly decreased when aggregating to cylinders, we quantitatively calculated the change of the specific surface area of the spherical micelles before and after the formation of cylinders. The relationship between the specific surface area of the cylinders and the spherical micelles was illustrated in Eq. (1). The detailed calculation process was presented in Supplementary information. The average radii of the spherical micelles and cylinders measured from TEM images are 12.4 and 34.3 nm, respectively. Therefore, the ratio of  $S_2$  to  $S_1$  equals to 0.241, which means that the total specific surface area of the spherical micelles decreased by 75.9% after CD-FIPA to form cylinders.

$$\frac{S_2}{S_1} = \frac{2r_1}{3r_2} \quad (1)$$

where  $r_1$  and  $r_2$  represent the average radii of the spherical micelles and the cylinders;  $S_1$  and  $S_2$  are the total specific surface areas of the spherical micelles and the cylinders.

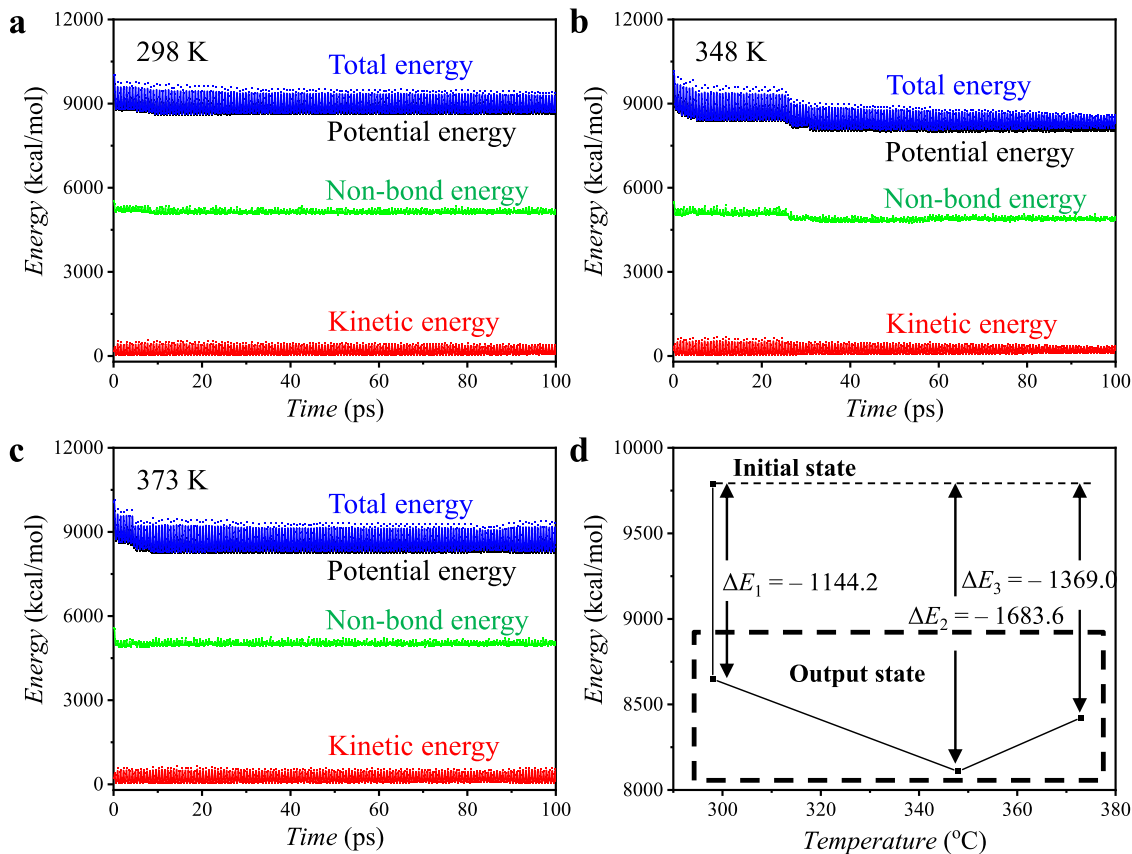


**Fig. 6** Energy evolution curves of PAzoMA<sub>5</sub> in a crystalline cell from MD simulations at different temperatures. **a** 298, **b** 348, and **c** 373 K. **d** Illustrative analysis of energy state and  $\Delta E$  calculated from MD simulations at 298, 348 and 373 K, respectively.

**Table 1** Summary of the radiuses of the cylinders and relative specific surface areas at different mass ratio of added micelles to cylinders.

Mass ratio of added micelles to cylinders ( <i>n</i> )	<i>r</i> <sub>1</sub> (nm)	<i>r</i> <sub>2</sub> (nm)	<i>r</i> <sub>3</sub> (nm)	Relative <i>S</i> <sup>a</sup>
0	12.4	–	–	0.241
1	12.4	34.3	47.1	0.370
2	12.4	47.1	59.2	0.376
3	12.4	59.2	68.8	0.455

<sup>a</sup>Relative total specific surface area of the cylinders after growth comparing to that before aggregation and fusion with the spherical micelles, which was obtained by  $S_3/(S_1 + S_2)$ .

In addition, we calculated the changes of the total specific surface area of the system before and after the lateral growth of cylinders. The following Eq. (2) was obtained and the detailed calculation process was also presented in the Supplementary information. The summary of the relative specific surface area of the cylinders after growth calculated from Eq. (2) was presented in Table 1. The mass ratio of added micelles to cylinders (*n*) of 0 means the CD-FIPA of the spherical micelles to form preformed cylinders, which has been discussed in the previous subsection. With the addition of spherical micelles to the solution of cylinders, the micelles attached onto and fused with the cylinders to form grown cylinders with increased diameters. The total specific surface area of the added micelles was decreased by 63.0% when fusing with the preformed cylinders for one time. Repeating this process, the living lateral growth of cylinders could be achieved. The relative specific surface areas of the grown cylinders

were decreased by 62.4% and 54.5% comparing with the total specific surface area of the added micelles and premature cylinders, respectively, demonstrating the lower surface free energy of the grown cylinder.

$$\frac{S_3}{S_1 + S_2} = \frac{2r_1r_3}{3(r_3^2 - r_2^2) + r_2} \quad (2)$$

where *r*<sub>1</sub> represents the average radiuses of the spherical micelles; *r*<sub>2</sub> and *r*<sub>3</sub> represent the average radiuses of the cylinders before and after growth; *S*<sub>1</sub>, *S*<sub>2</sub>, and *S*<sub>3</sub> are the total specific surface area of the added spherical micelles and the cylinders before and after growth, respectively.

In summary, a CD-FIPA strategy was proposed to prepare crystalline cylinders from amorphous micelles and control the living lateral growth of cylinders. Upon increasing temperature, the electrosteric stability of the spherical PAzoMA micelles was broken, leading to the aggregation and fusion of the micelles to form cylinders. It is worth noting that the cylinders are crystalline, which is different from amorphous spherical micelles due to the regular rearrangement of the azobenzene pendants when incubated at 75 °C. More importantly, the living lateral growth of the cylinders could be accomplished by further attaching and fusion of the added spherical micelles with the cylinders. The diameter of the cylinders could be controlled from 68.6 ± 12.3 to 137.6 ± 17.3 nm. Either from experimental observation or theoretical calculation, we confirmed that crystallization is the main driving force of CD-FIPA, and all the added micelles were attached and fused with the cylinders. MD simulations confirmed that the total energy of the system decreased sharply during the self-assembly and CD-FIPA processes, demonstrating the more stable thermodynamic state of the cylinders. Besides,



mathematical calculations also revealed that the total specific surface area of the cylinders were significantly decreased after CD-FIPA and lateral growth of the cylinders.

## Methods

**Reagents.** Anhydrous ethanol (AR), 4-(phenyldiazenyl)phenol (98%), 2-bromoethanol (95%),  $K_2CO_3$  (AR), methacryloyl chloride (95%), triethylamine (AR), tetrahydrofuran (THF, AR), dioxane (AR),  $NaHCO_3$  (AR), anhydrous  $Na_2SO_4$  (AR), ethyl acetate (AR), DMF (HPLC), 4,4'-azobis(4-cyanovaleric acid) (98%) and 4-cyano-4-((phenylcarbonothioyl)thio)pentanoic acid (HPLC, > 97%) were purchased from Aladdin.  $CDCl_3$  was purchased from J&K Scientific, Ltd. THF was dried via sodium before use, and other reagents were used without further purification.

**Synthesis of 2-(4-(phenyldiazenyl)phenoxy)ethanol.** 4-(Phenyldiazenyl)phenol (3.962 g, 20.00 mmol) and 2-bromoethanol (3.099 g, 25.00 mmol) was dissolved in 100 mL of anhydrous ethanol in a round bottom flask.  $K_2CO_3$  (3.455 g, 25.00 mmol) was added into the flask as acid binding agent. Then the dispersion was stirred at room temperature for 72 h. After reaction, the dispersion was filtered and dried under vacuum. The filter residue was dissolved in ethyl acetate and washed with saturated  $NaHCO_3$  and water for 3 times, respectively. The organic layer was dried via anhydrous  $Na_2SO_4$  and dried under vacuum after filtration. The obtained crude product was recrystallized in ethanol to give purified product.  $^1H$  NMR (400 MHz,  $CDCl_3$ ,  $\delta$ , ppm, Supplementary Fig. 2): 7.96–7.85 (m, 4H), 7.55–7.41 (m, 3H), 7.04 (d,  $J$  = 8.0 Hz, 2H), 4.16 (t,  $J$  = 4.0 Hz, 2H), 4.00 (t,  $J$  = 4.0 Hz, 2H).

**Synthesis of 2-(4-(phenyldiazenyl)phenoxy)ethyl methacrylate (AzoMA) monomer.** The obtained 2-(4-(phenyldiazenyl)phenoxy) ethanol (2.421 g, 10.00 mmol) and triethylamine (1.518, 15.00 mmol) were dissolved in 30 mL of anhydrous tetrahydrofuran in a round bottom flask. The temperature was cooled to 0–5 °C. Methacryloyl chloride (1.375 g, 15.00 mmol) was diluted in 10 mL of anhydrous tetrahydrofuran and dropped into the flask in 20 min. Then the solution was stirred at room temperature for 24 h. After reaction, the dispersion was filtered and dried under vacuum. The obtained powder was dissolved in ethyl acetate and washed with saturated  $NaHCO_3$  and water for 3 times, respectively. The organic layer was dried via anhydrous  $Na_2SO_4$  and dried under vacuum after filtration. The obtained crude product was purified by column chromatography (ethyl acetate/n-hexane = 1/3 (v/v)) to give AzoMA.  $^1H$  NMR (400 MHz,  $CDCl_3$ ,  $\delta$ , ppm, Supplementary Fig. 3a): 7.96–7.85 (m, 4H), 7.55–7.41 (m, 3H), 7.04 (d,  $J$  = 8.0 Hz, 2H), 6.16 (s, 1H), 5.60 (s, 1H), 4.53 (t,  $J$  = 4.0 Hz, 2H), 4.29 (t,  $J$  = 4.8 Hz, 2H), 1.96 (s, 3H).  $^{13}C$  NMR (400 MHz,  $CDCl_3$ ,  $\delta$ , ppm, Supplementary Fig. 3b): 167.30, 161.00, 152.74, 147.29, 135.95, 130.49, 129.06, 126.22, 124.78, 122.62, 114.89, 66.23, 62.93, 18.33. ESI-MS ( $m/z$ , Supplementary Fig. 3c):  $[M+H]^+$  calcd for  $C_{18}H_{18}N_2O_3$ ; 311.1351; found, 311.1383.

**Synthesis of PAzoMA.** The homopolymer PAzoMA was synthesized via RAFT polymerization according to the following procedures. CPAD (41.8 mg, 0.150 mmol), AzoMA (1.27 g, 3.75 mmol), and dioxane (2.0 mL) were added to a round bottom flask. Then oxygen was removed by filling with argon into the flask for 30 min. AIBN (3.70 mg, 0.0225 mmol) was rapidly added into the flask with bubbling for additional 5 min. Then the flask sealed with argon was placed in an oil bath at 70 °C. After 24 h, the reaction was terminated by cooling down to room temperature and exposing to air. The mixture was evaporated under vacuum to give a red-brown solid for further characterization.  $^1H$  NMR (400 MHz,  $CDCl_3$ ,  $\delta$ , ppm, Supplementary Fig. 4a): 7.89–7.70 (l, m, 4H,  $(NCCH)_4$ ), 7.49–7.33 (a, b, n, o, 3H,  $(CHCHCH)_3$ ), 6.99–6.74 (c, k, 1H,  $OCCHCH$ ), 4.40–3.83 (l, j, h, 4H,  $OCH_2CH_2O$ ), 2.09–0.74 (d–g, 5H,  $CCH_2C$ ,  $CCH_3$ ).  $^{13}C$  NMR (400 MHz,  $CDCl_3$ ,  $\delta$ , ppm, Supplementary Fig. 4b): 160.69, 152.60, 147.10, 130.49, 129.05, 124.77, 122.66, 114.68, 65.41, 63.18, 45.15, 44.80.

**Self-assembly of PAzoMA.** The PAzoMA was dissolved in 5.0 mL of THF with a concentration of 0.5 mg  $mL^{-1}$ , followed by adding deionized water (water/THF = 2:1 (v/v)) into the solution with a dropping rate of 0.5 mL  $min^{-1}$  under stirring. The THF was removed by dialyzing against deionized water for 2 days to afford aqueous solution of spherical micelles (0.12 mL  $min^{-1}$ ).

**Formation of cylinders via the incubation of spherical micelles.** The aqueous solution of spherical micelles with a concentration of 0.12 mg  $mL^{-1}$  was incubated in a water bath at 75 °C. At different incubation time, part of the solution was taken out and cooled naturally for further characterization.

**Living lateral growth of cylinders.** The aqueous solution of cylinders (0.12 mg  $mL^{-1}$ , 5 mL) was incubated in a water bath at 75 °C, then the aqueous solution of spherical micelles (0.12 mg  $mL^{-1}$ , 5 mL) was added into the solution and incubated for 3 h. After cooled to room temperature, the solution of cylinders with different diameters were obtained.

**Computer simulations.** *Materials Studio* 2017 was used for MD simulations. The model for polymer was respectively packed into an amorphous cell or a crystalline cell via the module of Amorphous Cell. The module of Forcite was used to simulate the molecular structure adaptation and energy fluctuation during the self-assembly process of PAzoMA, and crystalline cell was used to reveal the energy fluctuation in the crystallization-driven fusion-induced particle assembly (CD-FIPA) of the micelles. Forcite module was used for geo-optimization of PAzoMA, MD simulations and energy calculation. Firstly, the corresponding models of the polymers used for simulations were constructed and optimized. PAzoMA<sub>21</sub> was used for the calculation of the self-assembly process and PAzoMA<sub>5</sub> without terminal group was used to reveal the CD-FIPA process in order to simplify the calculation procedure. All constructed models were optimized by the module of Forcite upon construction. The Forcite optimization parameters were as follows: algorithm: smart; convergence tolerance: energy:  $1.0 \times 10^{-4}$  kcal  $mol^{-1}$ , force: 0.005 kcal  $mol^{-1} \text{ \AA}^{-1}$ , displacement:  $5.0 \times 10^{-5}$  Å; maximum number of iterations: 500; motion groups rigid: NO; forcefield: universal. To test the structure optimization and energy fluctuation of the polymers during the self-assembly, different cells were built with the module of Amorphous Cell, respectively. For the self-assembly of PAzoMA<sub>21</sub> to form micelles, five polymer chains were involved in one cell. While for the CD-FIPA process, one polymer chain was involved in the cell to simplify the calculation process. Afterward, the cell was calculated with dynamics under the parameters as follows: canonical (NVT); temperature: 298.00, 348.00, and 373.00 K; time step: 1.00 fs; number of steps: 50,000 or 100,000; and duration: 50 or 100 ps. The dynamics simulations were performed under universal forcefield. Energy evolution curves at different temperatures were obtained along with the simulation procedures. The energy data were obtained via the module of energy under Forcite to evaluate the corresponding energy changes of each cell quantitatively during the whole process of dynamics calculations.

## Data availability

All data needed to evaluate the conclusions of this study are available in the main text and Supplementary Information. The data supporting the findings of this work are available from the corresponding authors on request.

Received: 19 October 2021; Accepted: 4 April 2022;

Published online: 21 April 2022

## References

- Chen, G. & Jiang, M. Cyclodextrin-based inclusion complexation bridging supramolecular chemistry and macromolecular self-assembly. *Chem. Soc. Rev.* **40**, 2254–2266 (2011).
- Mai, Y. & Eisenberg, A. Self-assembly of block copolymers. *Chem. Soc. Rev.* **41**, 5969–5985 (2012).
- Blanazs, A., Armes, S. P. & Ryan, A. J. Self-assembled block copolymer aggregates: from micelles to vesicles and their biological applications. *Macromol. Rapid Commun.* **30**, 267–277 (2009).
- Varlas, S., Lawrenson, S. B., Arkinstall, L. A., O'Reilly, R. K. & Foster, J. C. Self-assembled nanostructures from amphiphilic block copolymers prepared via ring-opening metathesis polymerization (ROMP). *Prog. Polym. Sci.* **107**, 101278 (2020).
- Zhu, Y., Yang, B., Chen, S. & Du, J. Polymer vesicles: Mechanism, preparation, application, and responsive behavior. *Prog. Polym. Sci.* **64**, 1–22 (2017).
- Sun, H. & Du, J. Intramolecular cyclization-induced crystallization-driven self-assembly of an amorphous poly(amic acid). *Macromolecules* **53**, 11033–11039 (2020).
- Tian, Q., Fei, C., Yin, H. & Feng, Y. Stimuli-responsive polymer wormlike micelles. *Prog. Polym. Sci.* **89**, 108–132 (2019).
- Wan, X. et al. Drug combination synergy in worm-like polymeric micelles improves treatment outcome for small cell and non-small cell lung cancer. *ACS Nano* **12**, 2426–2439 (2018).
- Peng, J. et al. Herceptin-conjugated paclitaxel loaded PCL-PEG worm-like nanocrystal micelles for the combinatorial treatment of HER2-positive breast cancer. *Biomaterials* **222**, 119420 (2019).
- Wang, Y. et al. Worm-like biomimetic nanoerythrocyte carrying siRNA for melanoma gene therapy. *Small* **14**, 1803002 (2018).
- Hua, Z. et al. Anisotropic polymer nanoparticles with controlled dimensions from the morphological transformation of isotropic seeds. *Nat. Commun.* **10**, 5406 (2019).
- Du, Z.-X., Xu, J.-T. & Fan, Z.-Q. Micellar morphologies of poly( $\epsilon$ -caprolactone)-*b*-poly(ethylene oxide) block copolymers in water with a crystalline core. *Macromolecules* **40**, 7633–7637 (2007).
- Nazemi, A. et al. Monodisperse cylindrical micelles and block comicelles of controlled length in aqueous media. *J. Am. Chem. Soc.* **138**, 4484–4493 (2016).
- Ganda, S. & Stenzel, M. H. Concepts, fabrication methods and applications of living crystallization-driven self-assembly of block copolymers. *Prog. Polym. Sci.* **101**, 101195 (2020).



15. He, W.-N. & Xu, J.-T. Crystallization assisted self-assembly of semicrystalline block copolymers. *Prog. Polym. Sci.* **37**, 1350–1400 (2012).
16. Finnegan, J. R. et al. Extending the scope of “living” crystallization-driven self-assembly: self-defined 1D micelles and block comicelles from crystallizable polycarbonate block copolymers. *J. Am. Chem. Soc.* **140**, 17127–17140 (2018).
17. Jin, X.-H. et al. Long-range exciton transport in conjugated polymer nanofibers prepared by seeded growth. *Science* **360**, 897–900 (2018).
18. Nabyan, A., Biehl, P. & Schacher, F. H. Crystallization vs metal chelation: solution self-assembly of dual responsive block copolymers. *Macromolecules* **53**, 5056–5067 (2020).
19. Nie, J., Wang, Z., Huang, X., Lu, G. & Feng, C. Uniform continuous and segmented nanofibers containing a  $\pi$ -conjugated oligo(*p*-phenylene ethynylene) core via “living” crystallization-driven self-assembly: Importance of oligo(*p*-phenylene ethynylene) chain length. *Macromolecules* **53**, 6299–6313 (2020).
20. Hurst, P. J., Rakowski, A. M. & Patterson, J. P. Ring-opening polymerization-induced crystallization-driven self-assembly of poly-L-lactide-block-polyethylene glycol block copolymers (ROPI-CDSA). *Nat. Commun.* **11**, 4690–4690 (2020).
21. Hailes, R. L. N., Oliver, A. M., Gwyther, J., Whittell, G. R. & Manners, I. Polyferrocenylsilanes: synthesis, properties, and applications. *Chem. Soc. Rev.* **45**, 5358–5407 (2016).
22. Boott, C. E., Gwyther, J., Harniman, R. L., Hayward, D. W. & Manners, I. Scalable and uniform 1D nanoparticles by synchronous polymerization, crystallization and self-assembly. *Nat. Chem.* **9**, 785–792 (2017).
23. Rupar, P. A., Chabanne, L., Winnik, M. A. & Manners, I. Non-centrosymmetric cylindrical micelles by unidirectional growth. *Science* **337**, 559–562 (2012).
24. Li, X. Y., Gao, Y., Boott, C. E., Winnik, M. A. & Manners, I. Non-covalent synthesis of supermicelles with complex architectures using spatially confined hydrogen-bonding interactions. *Nat. Commun.* **6**, 8127 (2015).
25. He, Y. et al. Uniform biodegradable fiber-like micelles and block comicelles via “living” crystallization-driven self-assembly of poly(L-lactide) block copolymers: the importance of reducing unimer self-nucleation via hydrogen bond disruption. *J. Am. Chem. Soc.* **141**, 19088–19098 (2019).
26. Arno, M. C. et al. Precision epitaxy for aqueous 1D and 2D poly( $\epsilon$ -caprolactone) assemblies. *J. Am. Chem. Soc.* **139**, 16980–16985 (2017).
27. Yu, W., Foster, J. C., Dove, A. P. & O'Reilly, R. K. Length control of biodegradable fiber-like micelles via tuning solubility: a self-seeding crystallization-driven self-assembly of poly( $\epsilon$ -caprolactone)-containing triblock copolymers. *Macromolecules* **53**, 1514–1521 (2020).
28. Gao, L. et al. Growth and termination of cylindrical micelles via liquid-crystallization-driven self-assembly. *Macromolecules* **53**, 8992–8999 (2020).
29. Li, D. et al. Synthesis of AB<sub>n</sub>-type colloidal molecules by polymerization-induced particle-assembly (PIPA). *Chem. Sci.* **11**, 2855–2860 (2020).
30. Xiao, J. & Du, J. Tetrapod polymersomes. *J. Am. Chem. Soc.* **142**, 6569–6577 (2020).
31. Dou, J. et al. Fabrication of the polymersomes with unique and even nonequilibrium morphologies. *Macromol. Rapid Commun.* **42**, e2000504 (2021).
32. Zhang, Q. et al. Two polymersome evolution pathways in one polymerization-induced self-assembly (PISA) system. *Macromolecules* **53**, 8982–8991 (2020).
33. Varlas, S. et al. Polymerization-induced polymersome fusion. *J. Am. Chem. Soc.* **141**, 20234–20248 (2019).
34. Zhang, X. et al. Giant polymer vesicles with a latticelike membrane. *ACS Macro Lett.* **10**, 1015–1022 (2021).
35. Kuenstler, A. S., Clark, K. D., Read de Alaniz, J. & Hayward, R. C. Reversible actuation via photoisomerization-induced melting of a semicrystalline poly(azobenzene). *ACS Macro Lett.* **9**, 902–909 (2020).
36. Tong, Z. et al. Spatially restricted templated growth of poly( $\epsilon$ -caprolactone) from carbon nanotubes by crystallization-driven self-assembly. *Macromolecules* **54**, 2844–2851 (2021).
37. Mandelkern, L. *Crystallization of Polymers* 2nd edn (Cambridge University Press, Cambridge, 2002).
38. Ishiba, K. et al. Photoliquefiable ionic crystals: a phase crossover approach for photon energy storage materials with functional multiplicity. *Angew. Chem. Int. Ed.* **54**, 1532–1536 (2015).
39. Li, J., Wang, M. W., Liu, Y., Ren, W. M. & Lu, X. B. Photoinduced reversible semicrystalline-to-amorphous state transitions of stereoregular azopolyesters. *Angew. Chem. Int. Ed.* **60**, 17898–17903 (2021).
40. Appiah, C., Woltersdorf, G., Pérez-Camargo, R. A., Müller, A. J. & Binder, W. H. Crystallization behavior of precision polymers containing azobenzene defects. *Eur. Polym. J.* **97**, 299–307 (2017).
41. Du, J., Willcock, H., Patterson, J. P., Portman, I. & O'Reilly, R. K. Self-assembly of hydrophilic homopolymers: a matter of RAFT end groups. *Small* **7**, 2070–2080 (2011).
42. Xu, J., Tao, L., Boyer, C., Lowe, A. B. & Davis, T. P. Facile access to polymeric vesicular nanostructures: remarkable  $\omega$ -End group effects in cholesterol and pyrene functional (Co)polymers. *Macromolecules* **44**, 299–312 (2011).
43. Sun, H., Liu, D. & Du, J. Nanobowls with controlled openings and interior holes driven by the synergy of hydrogen bonding and  $\pi$ - $\pi$  interaction. *Chem. Sci.* **10**, 657–664 (2019).
44. Tian, L., Ren, Y., Yang, R., Zhao, Q. & Zhang, W. Combination of thermal pretreatment and alcohol-assisted aqueous processing for rapeseed oil extraction. *J. Sci. Food Agric.* **99**, 3509–3516 (2019).
45. Zhong, J., Luo, H., Tang, Q., Lei, Z. & Tong, Z. Counterion-mediated self-assembly of ion-containing block copolymers on the basis of the Hofmeister series. *Macromol. Chem. Phys.* **220**, 1800554 (2019).
46. Chen, S., Qin, J. & Du, J. Two principles for polymersomes with ultrahigh biomacromolecular loading efficiencies: acid-induced adsorption and affinity-enhanced attraction. *Macromolecules* **53**, 3978–3993 (2020).
47. van Gunsteren, W. F. & Berendsen, H. J. C. Computer simulation of molecular dynamics: methodology, applications, and perspectives in chemistry. *Angew. Chem. Int. Ed.* **29**, 992–1023 (1990).

## Acknowledgements

This work was supported by Natural Science Foundation of Ningxia (2021AAC03026 and 2020AAC03003). H.S. thanks the Ningxia Youth Talent Support Project of Science and Technology and Young Scholars of Western China of CAS. J.D. is a recipient of National Science Fund for Distinguished Young Scholars, NSFC (21925505), and supported by Shanghai international scientific collaboration fund (21520710100). We appreciate Dr. Xinhua Gao in Ningxia University for helping XRD tests.

## Author contributions

H.S. and J.D. conceived the subject and organized the work. X.L. and X.Z. performed the synthesis and characterization of the polymers and nanostructures. S.C. contributed to the MD simulations. Y.L. carried out the DLS and SEM characterizations. H.S. drafted the manuscript and co-revised it with J.D.

## Competing interests

The authors declare no competing interests.

## Additional information

**Supplementary information** The online version contains supplementary material available at <https://doi.org/10.1038/s41467-022-29863-8>.

**Correspondence** and requests for materials should be addressed to Hui Sun or Jianzhong Du.

**Peer review information** *Nature Communications* thanks Xiao-Song Wang and the other anonymous reviewer(s) for their contribution to the peer review of this work.

**Reprints and permission information** is available at <http://www.nature.com/reprints>

**Publisher's note** Springer Nature remains neutral with regard to jurisdictional claims in published maps and institutional affiliations.



**Open Access** This article is licensed under a Creative Commons Attribution 4.0 International License, which permits use, sharing, adaptation, distribution and reproduction in any medium or format, as long as you give appropriate credit to the original author(s) and the source, provide a link to the Creative Commons license, and indicate if changes were made. The images or other third party material in this article are included in the article's Creative Commons license, unless indicated otherwise in a credit line to the material. If material is not included in the article's Creative Commons license and your intended use is not permitted by statutory regulation or exceeds the permitted use, you will need to obtain permission directly from the copyright holder. To view a copy of this license, visit <http://creativecommons.org/licenses/by/4.0/>.

© The Author(s) 2022